REVIEW ARTICLE

In situ synchrotron based x-ray techniques as monitoring tools for atomic layer deposition

Kilian Devloo-Casier[a)]
Department of Solid State Sciences, Ghent University, Krijgslaan 281/S1, B-9000 Ghent, Belgium

Karl F. Ludwig
Physics Department, Boston University, 590 Commonwealth Avenue, Boston, Massachusetts 02215

Christophe Detavernier and Jolien Dendooven
Department of Solid State Sciences, Ghent University, Krijgslaan 281/S1, B-9000 Ghent, Belgium

(Received 5 November 2013; accepted 5 December 2013; published 26 December 2013)

Atomic layer deposition (ALD) is a thin film deposition technique that has been studied with a variety of *in situ* techniques. By exploiting the high photon flux and energy tunability of synchrotron based x-rays, a variety of new *in situ* techniques become available. X-ray reflectivity, grazing incidence small angle x-ray scattering, x-ray diffraction, x-ray fluorescence, x-ray absorption spectroscopy, and x-ray photoelectron spectroscopy are reviewed as possible *in situ* techniques during ALD. All these techniques are especially sensitive to changes on the (sub-)nanometer scale, allowing a unique insight into different aspects of the ALD growth mechanisms. © *2014 American Vacuum Society*. [http://dx.doi.org/10.1116/1.4851716]

I. INTRODUCTION

Atomic layer deposition (ALD) is a thin film deposition technique, which enables thickness control at the atomic level and conformal deposition on high aspect ratio structures.[1–4] The unique properties of ALD are achieved by using self-terminating reactions between precursor molecules and the surface. Typically, two different precursor vapors or gases are used. They are sequentially introduced to the reaction chamber. Between the exposures, the chamber is either purged with an inert gas or evacuated. This prevents unwanted gas phase reactions and removes reaction products from the chamber. The precursor chemistry is optimized to ensure saturation of the surface with precursor molecules after every half cycle. Because an ALD process consists of very well defined steps, it is a process that allows for a detailed study of the involved mechanisms during growth.

A wide range of characterization techniques have been implemented on ALD reactors, enabling *in situ* monitoring of growth. They can be grouped into different categories, based on the properties that are measured. A first category directly monitors physical changes. Examples are quartz crystal microbalance[5–8] measuring mass change, four-point probe[9] measuring electronic resistivity, and thermopile[10] measuring the reaction enthalpies. A second category of techniques probes the gas species that are being consumed and formed during the various chemical reactions involved in the ALD process. Examples are quadrupole mass spectrometry,[7,8,11] optical emission spectroscopy,[12,13] and Fourier transformed infrared (FTIR) absorption spectroscopy.[14] A last category uses light from either the infrared or visual range to monitor the optical properties of the surface and/or the deposited layer. Examples are surface photoabsorption,[15,16] FTIR absorption,[17–19] spectroscopic ellipsometry,[20] and ellipsometric porosimetry.[21] These optical techniques are the easiest to use in practice, since no measuring equipment needs to be incorporated within the ALD chamber. They can remotely probe the sample surface and only require an entry and exit window to pass light into and out of the reactor chamber.

The relatively easy incorporation of light based techniques into ALD research has encouraged the exploration of the possibilities for wavelengths from the IR to the UV. The aim of this paper is to show that this wavelength range can be expanded to x-rays, opening up an even wider variety of characterization possibilities. Although standard x-ray based analysis techniques such as x-ray reflectivity and diffraction using lab-based x-ray sources have proven valuable for *ex situ* characterization of ALD deposited thin films, most *in situ* experiments during ALD require synchrotron-based x-rays. To enable *in situ* studies during ALD, it is important to limit the impact of the prolonged purge or evacuation times that are introduced between subsequent ALD (half-) cycles to perform the measurements. The high photon flux at a synchrotron facility is beneficial in this respect, because it allows for shorter acquisition times compared to lab-based x-ray sources. The high intensity x-ray flux also lowers the detection limit, enabling the study of layer growth from the very first ALD cycle onward. A second main advantage of synchrotron sources is its unique ability to tune the photon energy to a specific experiment and material system. Additionally, as shown in Table I, the use of synchrotron

a)Electronic mail: Kilian.DevlooCasier@Ugent.be

TABLE I. Available *in situ* characterization methods when using synchrotron radiation and the primary sample properties, important to ALD research, that become accessible.

Technique	Accessible information	References
XRR	Thickness	22–27
	Roughness	
	Electron density	
GISAXS	Morphology	28
	Roughness	29
XRD	Phase and size of crystalline grains	30 and 31
XRF	Composition	26, 29, 32–35
EXAFS (*in vacuo*)	Local atomic environment	36–41
XPS (*in vacuo*)	Chemical state	37, 38, 42–45

based x-rays broadens the available tool box of *in situ* methods to a number of techniques, which are synchrotron specific, such as x-ray absorption spectroscopy (XAS) and grazing incidence small angle x-ray scattering (GISAXS). The table also includes the most important references reporting the *in situ* use of the respective technique during ALD.

This manuscript is intended as a tutorial review of *in situ* x-ray techniques as monitoring tool for ALD. In the following sections, the techniques mentioned in Table I will be briefly introduced and their possibilities will be illustrated with examples. Note that we do not intend to review the methods in detail, but rather want to demonstrate the specific advantages of these techniques as *in situ* analysis tool for ALD growth. Also, certain practical constraints and difficulties will be addressed.

II. EXPERIMENT

The *in situ* experiments presented in this paper have been performed in the UHV thin film growth facility installed at beamline X21 of the National Synchrotron Light Source at Brookhaven National Laboratory.[46] This setup consists of a stainless steel reaction chamber pumped by a turbo molecular pump to a base pressure of 10^{-6} mbar (Fig. 1). Samples can be introduced via a loadlock and mounted vertically in front of a resistive heating plate. The chamber is equipped with an entrance beryllium window for the transmission of the x-rays provided by the synchrotron, and two exit beryllium windows for the transmission and detection of the reflected, scattered, and fluorescent x-rays from the sample. A Vortex silicon drift detector mounted perpendicular to the sample surface is available to collect the fluorescence, while 2D scattering intensity maps can be recorded using a Dectris, Pilatus 100 k, 2D area detector mounted parallel to the sample. The whole chamber is mounted on a rotatable table, to allow tuning of the incidence angle to fit the experiment.

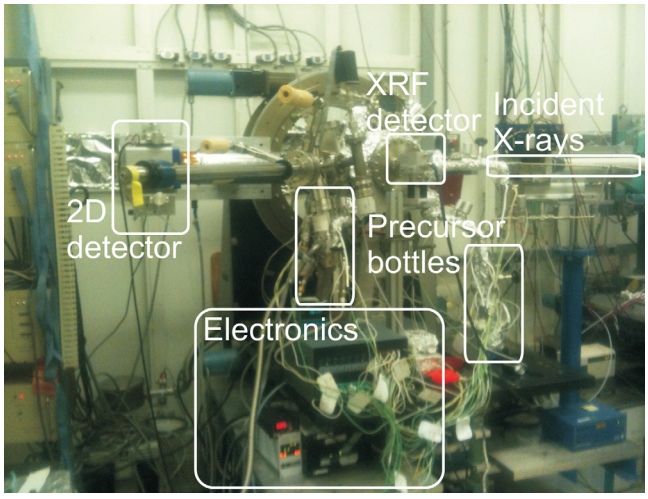

FIG. 1. (Color online) UHV film growth facility, adapted for thermal ALD, installed at beamline X21 of the National Synchrotron Light Source at Brookhaven National Laboratory.

Enabling thermal ALD of oxides in this setup required, among other things, the connection of precursor supply lines. H_2O vapor was used as oxygen source, while Table II lists the precursors that were used as metal source for the respective oxides. The delivery lines were equipped with needle valves to control the flow and pneumatic valves to regulate the gas inlet. For all processes, the exposure and pumping times were chosen long enough to ensure saturation and prevent CVD reactions, respectively. During the exposures, the pressure in the chamber was usually ca. 5 10^{-3} mbar. In the case of tetrakisethylmethylaminohafnium (TEMAH) and tetrakisdimethylaminotitanium (TDMAT), Ar was used as a carrier gas to compensate for the low vapor pressure of these materials. Finally, to avoid condensation of the precursors, the delivery lines and chamber walls were heated to 60 °C and 80 °C, respectively.

Besides for the study of metal oxide ALD processes, synchrotron-based x-ray techniques are extremely useful to investigate ALD of metals. To demonstrate this, and because of the incompatibility of the setup at beamline X21 with metal ALD, *ex situ* proof-of-principle experiments were performed on home-deposited Pt samples. These samples were prepared using the earlier reported (methylcyclopentadienyl) trimethylplatinum (MeCpPtMe3)/ozone process.[47]

III. SCATTERING BASED TECHNIQUES

A. X-ray reflectivity

X-ray reflectivity (XRR) is widely used in the determination of thickness, roughness, and density of thin films.[48] XRR measures the intensity of an x-ray beam that is specularly reflected from a surface as a function of the incident angle (typically from 0° to 3°). The complex refractive index (n) for x-rays is slightly smaller than 1

$$n = 1 - \delta + i\beta. \quad (1)$$

TABLE II. Deposited oxides with the used metal source. For TEMAH and TDMAT, argon is used as a carrier gas.

Oxide	Metal source
Al_2O_3	TMA
ZnO	Diethylzinc (DEZ)
HfO_2	TEMAH
TiO_2	TDMAT

Hence, total external reflection occurs at low angles. This allows the determination of the critical angle of the studied material. The critical angle (α_c) is directly linked to the electron density (n_e) of the reflecting medium

$$\alpha_c = \sqrt{2\delta} \approx \sqrt{2\frac{r_0\lambda^2}{2\pi}n_e}, \quad (2)$$

where r_0 is the Bohr atomic radius and λ the x-ray wavelength. Above the critical angle, the incident x-rays penetrate the film and the intensity of the reflected beam rapidly decreases with the angle. The use of synchrotron radiation increases the intensity of the incident and corresponding reflected beam. Therefore, compared to a lab based system, the maximum angle accessible will be increased with a couple degrees. The x-rays that penetrate the thin film will be reflected at the thin film/substrate interface. Together with the x-rays reflected at the air/film interface, this will create an interference pattern. These periodic oscillations in the XRR pattern, also known as Kiessig fringes, allow the determination of the film thickness (order 1–100 nm). If the surface is rough, the intensity of the reflected x-rays will drop off faster for increasing angles. The interface roughness will reduce the amplitude of the fringes. The difference in density between the film and the support will also influence the amplitude of the fringes.[49] Film thickness, roughness, and density are normally determined by fitting the measured curve to a theoretical model, like Parratts formalism.[50]

Since thin films grown by ALD are in most cases only a few nanometers thick and relatively smooth, XRR is ideally suited to study properties of growing ALD films. Because of the obvious link to thin film research, XRR was the first synchrotron based technique that has been utilized in ALD research to study high dielectric constant alumina thin films.[22] Since then several groups have adopted the technique into ALD research.[23–27]

In order to be useful as an *in situ* technique, XRR needs to be sensitive to changes in thickness and roughness on the order of Ångstroms and changes to the density of a few percent. Figure 2 aims to demonstrate the sensitivity of XRR. The simulations show that changes in the thickness of the Al_2O_3 film of the order of 1 Å can easily be distinguished by their change in oscillation period. The influence of a small roughness variation and a small change in layer density are shown to have a noticeable effect on the XRR pattern. From the simulations, it is also clear that a lab source, with a typical range up to 3°, is not sufficient to study layers with a thickness of 25 Å (or less). The higher intensity and corresponding larger angular range of synchrotron radiation is therefore needed for *in situ* studies of the very first stages of growth during ALD.[26]

To illustrate the possibilities of XRR as an *in situ* technique during ALD, we will discuss results obtained during the growth of Al_2O_3 on native SiO_2, followed by the growth of TiO_2 on top of the alumina. In Fig. 3, the measured XRR pattern is shown for the bare substrate, after 30 and 80 ALD cycles of Al_2O_3 and subsequently 40 ALD cycles of TiO_2.

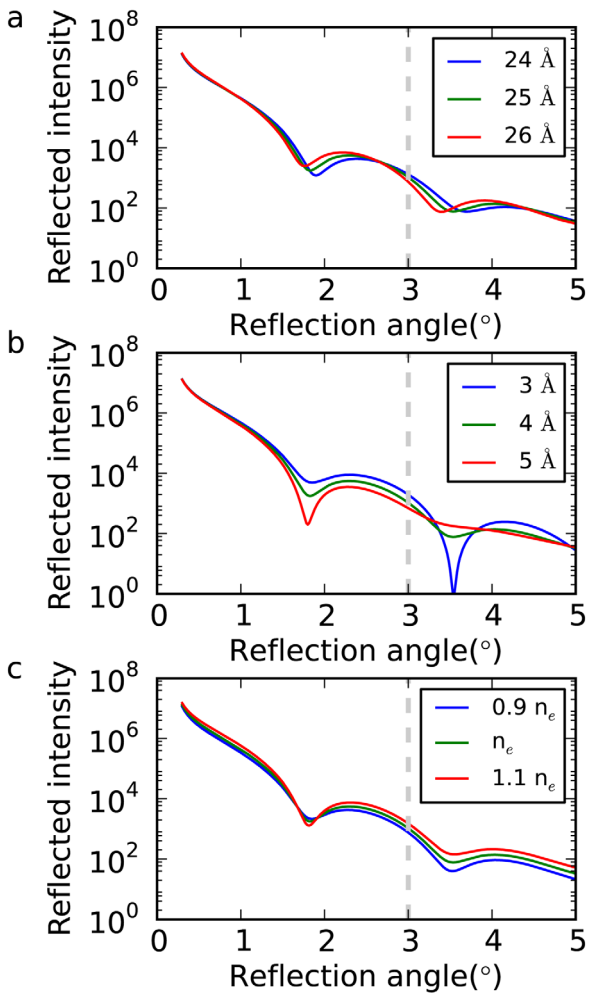

FIG. 2. (Color online) Simulated XRR patterns for Al_2O_3 on silicon. The parameters of the Al_2O_3 are changed to show the sensitivity to changes of interest during an ALD experiment. The angular range available to a lab based setup is marked with the dashed line indicating the need for synchrotron radiation at low layer thicknesses. (a) The sensitivity of XRR to thickness variations, (b) the sensitivity of XRR to roughness variations, and (c) the sensitivity of XRR to density variations in respect to the bulk density of Al_2O_3 (n_e).

From the decrease of the period of the fringes, it is clear that the layer is getting thicker with increasing ALD cycles. In Table III, the thickness, roughness, and density are given for each step, based on a fit to a theoretical model. It is important to note that the measurement after 30 ALD cycles of Al_2O_3 would not give the desired information if a lab based source would be used instead of the used synchrotron radiation as the angular range available at a lab based setup is limited to about 3°.

From the obtained values, one can see a clear increase in thickness, as can be expected from the standard Al_2O_3 process. The growth per cycle (GPC) can be calculated to be about 0.8 Å per cycle between ALD cycle 30 and 80. During the first 30 ALD cycles, however, the growth rate is lower, and the film density is low compared to bulk values for Al_2O_3. This points to nucleation effects related to the starting surface. During the following cycles, the film densifies to the expected value. Both the interface and surface roughness are

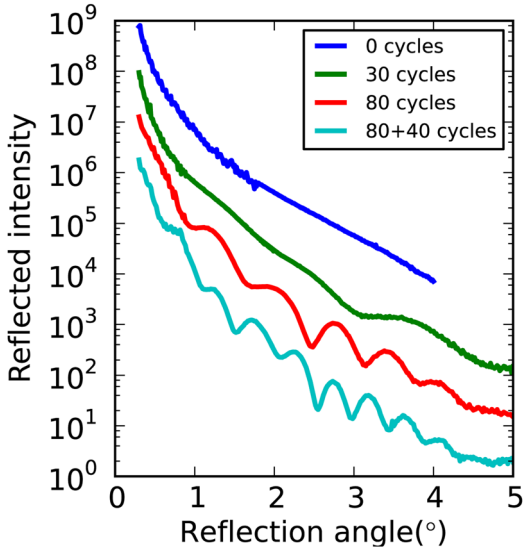

FIG. 3. (Color online) XRR pattern measured after, respectively, 30 and 80 ALD cycles of Al_2O_3 and subsequently 40 ALD cycles of TiO_2. The measurements are shifted vertically with respect to each other for clarity.

low and do not change a lot during deposition. The data here are only shown as an example, but an experiment with a higher frequency in measurements could provide a lot of extra insight in the evolution of thickness, roughness, and density.

When determining the properties of the TiO_2 layer, an added advantage of *in situ* XRR to *ex situ* XRR becomes apparent. An XRR pattern for a multilayer of materials is in most cases rather complex, since it contains contributions from every layer. The analysis can therefore be very difficult. Here the values obtained for the Al_2O_3 can be used as input parameters for the model of the multilayer. For even more complex multilayers, when an *in situ* XRR measurement is performed after the completion of every layer, the parameters for that layer can be determined and used as input parameters for the analysis of the more complex structure with an additional layer. This makes the analysis of the final structure a lot more straightforward and increases the accuracy, since only a limited set of parameters needs to be fitted at a time.

B. Grazing incidence small angle x-ray scattering

GISAXS is a powerful technique for the morphological characterization of nanoscale objects (particles, pores, etc.) at surfaces, at buried interfaces, or in thin films. Although the technique was originally introduced in 1989,[51] it was only in the past decade with the increasing interest in nanostructured surfaces and films that GISAXS has gained popularity as a structural characterization technique, as illustrated in a recent review paper.[52] GISAXS yields nanometer scale information averaged over a macroscopic sample area and allows to asses buried structures in a non-destructive way. Because no special sample preparation is required, GISAXS is also suitable for *in situ* experiments. High-brilliance synchrotron radiation is, however, almost a prerequisite. One of the main drawbacks of the technique is that the morphological information is obtained in reciprocal space. Because of refraction and reflection effects, the interpretation of GISAXS images in real-space can be ambiguous.

TABLE III. Values for thickness, roughness and density obtained by fitting the XRR patterns shown in Fig. 3.

ALD cycles	30 cycles	80 cycles	80 + 40 cycles
Interface roughness (Å)	2.5	1.4	1.4
Al_2O_3 thickness (Å)	15.5	55.3	55.3
Al_2O_3 roughness (Å)	2.4	2.5	2.5
Al_2O_3 density (g/cm^3)	2.68	3.67	3.67
TiO_2 thickness (Å)			33.0
TiO_2 roughness (Å)			3.1
TiO_2 density (g/cm^3)			4.39

A GISAXS experiment essentially consists of measuring the diffuse scattering around the specularly reflected beam at a fixed angle of incidence (Fig. 4). In order to reduce the unwanted bulk scattering from the substrate and to enhance the near-surface scattering, the incident angle, α_i, is kept very small with respect to the sample surface. In this geometry, any kind of roughness or electron density contrast in the (sub)surface region of the sample leads to scattering in off-specular directions. The scattered intensity is usually recorded by a 2D detector (located at 1−4 m from the sample) as a function of the out-of-plane angle α_f and the in-plane angle $2\theta_f$. To prevent saturation, or even damage, of the detector, the direct and specularly reflected beam, which have an intensity of several orders of magnitude higher than the diffuse scattering, are masked by slits or beamstops. Because the scattered x-rays are low in intensity, scattering from the direct beam at the entrance window to the chamber needs to be blocked with a carefully positioned knife edge between the entrance window and the sample. Similarly, the

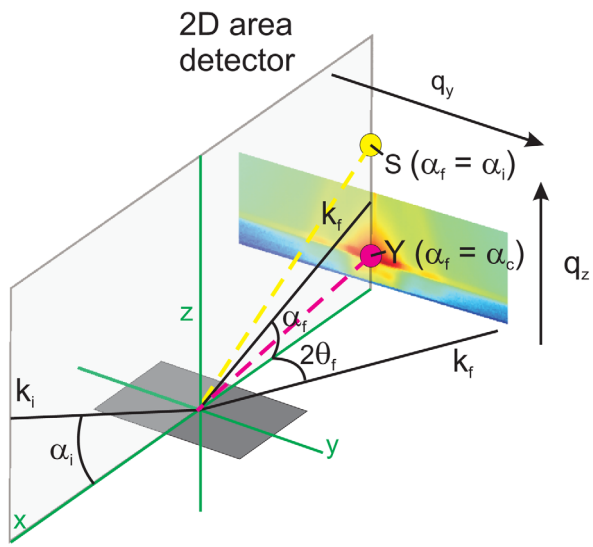

FIG. 4. (Color online) Schematics of the GISAXS geometry. Incident x-rays have a wavevector $\mathbf{k}_i$. Due to scattering the wavevector changes to $\mathbf{k}_f$. The momentum transfer due to scattering is denoted as $\mathbf{q}$. The position of the Yoneda peak has been marked with Y and the position of the reflected beam has been marked with S.

specularly reflected beam is preferably blocked prior to hitting the exit window.

In order to deduce morphological information from the measured 2D scattering patterns, the scattering vector **q** is defined as $\mathbf{k}_f - \mathbf{k}_i$, with $\mathbf{k}_i$ and $\mathbf{k}_f$ the wavevectors of the incident and scattered beams, respectively. The scattering vector components q_x, q_y, and q_z are related to the angles α_i, α_f and $2\theta_f$ by

$$\begin{aligned} q_x &= k_0\left[\cos(2\theta_f)\cos(\alpha_f) - \cos(\alpha_i)\right] \\ q_y &= k_0\left[\sin(2\theta_f)\cos(\alpha_f)\right] \\ q_z &= k_0\left[\sin(\alpha_f) + \sin(\alpha_i)\right] \\ k_0 &= |\mathbf{k}_i| = |\mathbf{k}_f| = 2\pi/\lambda. \end{aligned} \tag{3}$$

Because the angles are limited to a few degrees, the scattering vector components are also small, i.e., between 0 and a few nm^{-1}, meaning that dimensions from a few up to hundreds of nanometers are probed in real space.[53] Variation in the scattering intensity with q_y provides in-plane (lateral) structural information, while intensity variation with q_z provides out-of-plane (normal) structural information. Full analysis of the 2D GISAXS spectra can provide information on the geometry, size distribution, and spatial correlation of the scattering features.

If the exit angle equals the critical angle, an enhancement of the scattered intensity arises.[54] The so-called Yoneda peak is a typical dynamic feature of diffuse scattering. Because the critical angle is related to the electron density of the scattering medium, the Yoneda peak is a material dependent feature.

GISAXS can be useful in ALD research to study a range of very different problems. First, GISAXS can be used to study thin film growth on planar surfaces. In this case, the scattering can provide information on the evolution of surface roughness during growth. This has already been shown in a study of the initial growth of HfO_2 on Si and Ge substrates.[29] Second, in the case of, for example, metal ALD, where islands of material are being formed during the initial stages of growth, GISAXS allows for the analysis of the size, shape, and interparticle spacing. This can be very important in, e.g., the determination of particle size and dispersion for catalyst preparation by ALD. Third, GISAXS is frequently used to study nanostructured features at surfaces such as nanoporous layers or quantum dots.[55,56] These structures will have a very distinctive GISAXS pattern. When ALD is used in combination with these materials, the changes in scattering can be used to study, e.g., conformality and pore filling.

To show the power of GISAXS in ALD research, three examples will be discussed. All experiments used a similar geometry, working at an incident angle α_i of 0.8° in the first two examples and at an incident angle α_i of 1° for the third example. A PILATUS 100 K, 2D detector was used to measure the scattered x-rays, positioned approximately 1 m away from the sample. All measurements were performed at an x-ray energy of 10 keV.

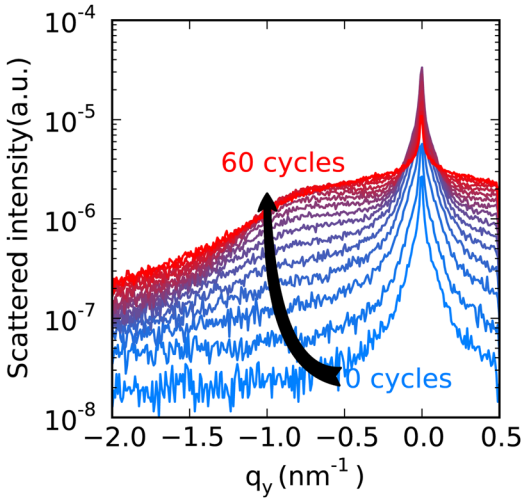

FIG. 5. (Color online) Evolution of the scattering intensity for low q_z ($\alpha_f = 0.2°$, $q_z = 0.88\,nm^{-1}$), as measured every four ALD cycles during ALD of HfO_2 on an Al_2O_3 surface.

In a first example, *in situ* GISAXS is used to study the evolution of the surface roughness during growth of a HfO_2 layer on a ALD grown Al_2O_3 surface. The evolution of the scattered intensity for low q_z ($\alpha_f = 0.2°$, $q_z = 0.88\,nm^{-1}$) during ALD is displayed in Fig. 5.

In the low q_z limit, the weighted integral of the GISAXS intensity can be used as a measure for the square of the rms roughness[57]

$$\sigma_{rms}^2 \propto \int q_{//} I(q_{//}) dq_{//}. \tag{4}$$

This enables a qualitative view on the roughness evolution during ALD deposition. In Fig. 6, the square root of the integral from Eq. (4) is shown as a function of ALD cycles.

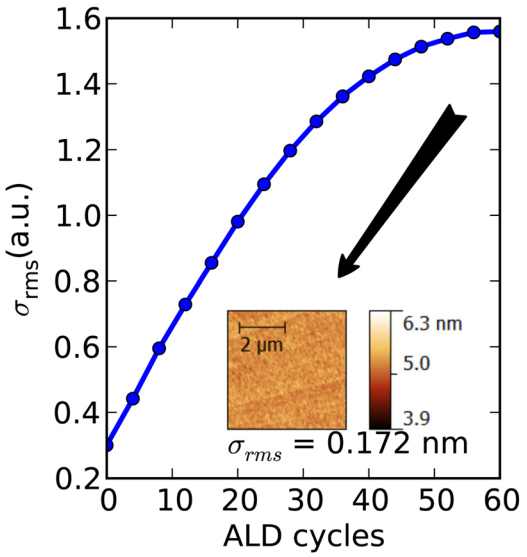

FIG. 6. (Color online) Qualitative evolution of roughness during HfO_2 growth based on the scattered intensity, calculated using Eq. (4). The AFM image at the end of the growth is included as an inset, with the corresponding σ_{rms} as determined from the AFM image.

A clear evolution in roughness can be seen. During the first ALD cycles, the surface roughness increases and stabilizes after several ALD cycles.

The second example concerns a proof of principle. Up until now, no *in situ* GISAXS measurements have been reported during metal ALD. Here, we will discuss the GISAXS pattern obtained for various stages of Pt growth on native SiO_2. These measurements were not performed during ALD growth itself, but were measured on a set of preprepared samples. The Pt has been grown using a thermal ALD process at 150 °C.[47] Similar experiments have already been reported for the growth of Pt on $SrTiO_3$.[58]

Platinum is known to form islands during the very first stages of growth, due to slow nucleation on nonmetallic surfaces. These islands or clusters will be distributed over the surface at random intervals and have a certain size distribution. As GISAXS looks at a macroscopic sized area of the substrate, the scattering contributions of many individual islands will get averaged out to show a mean distance and/or size of the island. In Fig. 7, the scattering pattern is shown for 30, 60, and 100 ALD cycles. A qualitative analysis of the patterns can already offer some insight. The GISAXS pattern for 30 ALD cycles only shows the Yoneda peak around the critical angle of silicon ($\alpha_c = 0.18°$, $q_z = 0.86\,nm^{-1}$), indicating that the silicon substrate is responsible for most scattering and hence that not a lot of growth has occurred. After 60 ALD cycles, two lobes appear, which hint in the direction of particle formation on the surface. Finally, after 100 ALD cycles, the lobes have shifted to smaller q_y values, indicating that larger particles have been formed. The position of the Yoneda wing has also shifted to higher q_z (in other words also higher α_f), corresponding to the higher critical angle for a platinum layer ($\alpha_c = 0.46°$, $q_z = 1.12\,nm^{-1}$). The position of the lobes can be used to determine the average interparticle spacing and shape of the particles. To obtain these values, patterns can be modeled using specific software (e.g., GISAXS[59]), but this is out of the scope of this article.

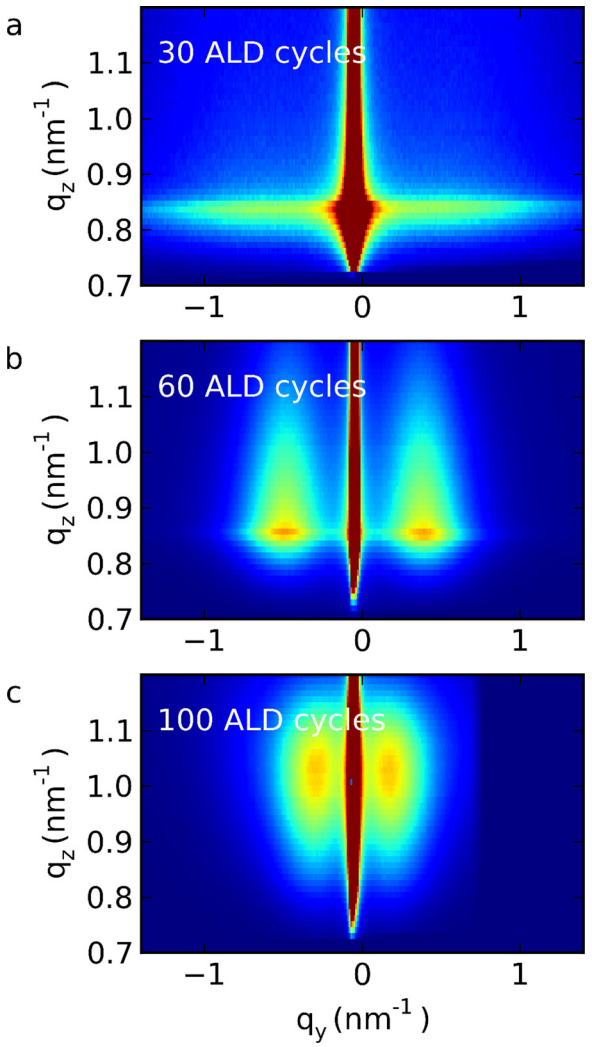

FIG. 7. (Color online) GISAXS patterns measured after respectively 30 ALD cycles (a), 60 ALD cycles (b), and 100 ALD cycles (c) of ozone based Pt deposition on Si. The appearance of lobes in the scattering pattern indicates the formation of islands. A shift of the critical angle can also be seen. The samples were prepared in the lab and studied *ex situ* in the setup at beamline X21 at Brookhaven National Laboratory.

A third example illustrates the use of GISAXS to study conformal ALD in complex nanostructures. Here, GISAXS was used to analyze the growth of ZnO in a porous silica film on a silicon support. The porous silica film has mesopores of the order of several nanometers. As has already been shown in literature,[21,34,60] these structures can be either conformally coated with ALD or the pores can be sealed. To ensure a large enough penetration depth for the x-rays, and incident angle of 1° was chosen for these experiments, instead of the previously used incident angle of 0.8°. When we look at the GISAXS pattern of the uncoated porous silica film (see Fig. 8), we see a very distinctive pattern. The Yoneda peak is clearly visible, as is a semicircle. This semicircle can be attributed to the ordered pores in the substrate. This is due to an interference effect of x-rays scattering at the pores' internal surface, due to the difference in refractive index. As the film gets gradually filled with ZnO, the Yoneda peak shifts to higher q_z values. This indicates a densification of the film as more and more ZnO gets incorporated into the porous structure. A change in the intensity corresponding to the scattering of the internal surface can be observed. As the contrast in refractive index changes due to the higher electron density of ZnO, the scattering pattern is influenced. After the ZnO deposition, the Yoneda peak has shifted to a value corresponding with the higher electron density of ZnO, and the semicircle is still present indicating the change from open pores to filled pores.

IV. X-RAY DIFFRACTION

X-ray diffraction (XRD) is one of the most widely used techniques in solid state sciences and materials research. The use of XRD enables the study of crystalline materials. As most materials deposited with ALD are amorphous during deposition, *in situ* XRD is limited to certain ALD processes. The most well-known oxide deposited with ALD that is crystalline during deposition is ZnO.[61] Most metals can also readily be studied with XRD. XRD has only been used a few

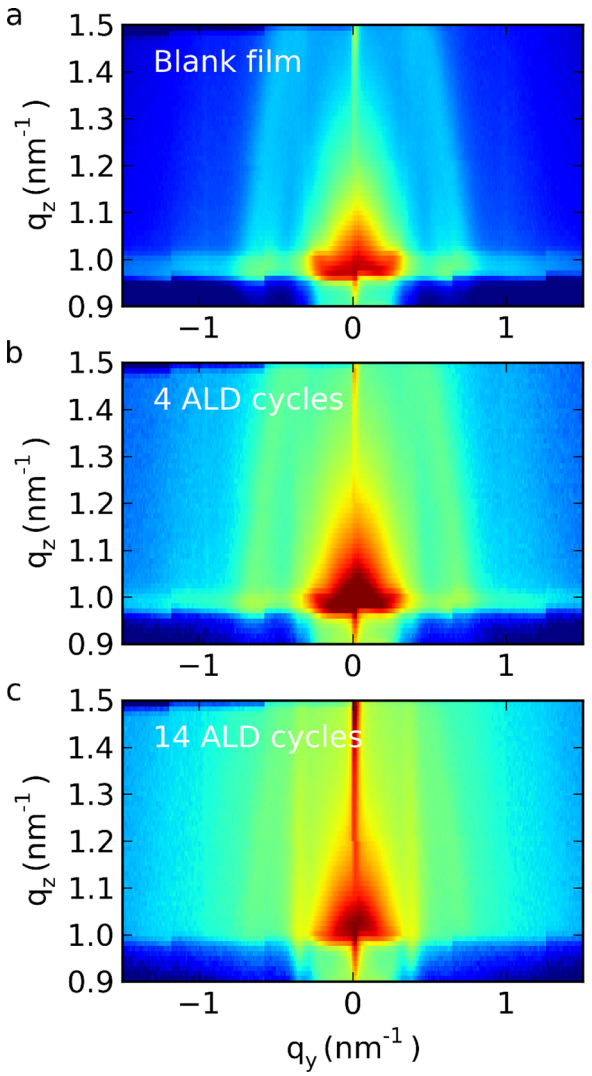

FIG. 8. (Color online) *In situ* GISAXS pattern for a porous silica film before deposition (a), after four ALD cycles (b) and after 14 ALD cycles (c) of DeZ and H_2O, respectively. A scattering pattern corresponding to the porous film can be seen. The shift of the critical angle shows the densification of the film by filling the porous structure.

times as an *in situ* technique.[24,31] There are however numerous examples of synchrotron based *ex situ* XRD studies on ALD grown layers.[30,62–66] This indicates that synchrotron based XRD has several advantages to lab based XRD. The main advantage is the lower detection limit. As the signal to noise ratio can be greatly increased when using the high photon flux at a synchrotron, even very small amounts of crystalline material can be detected. The lower divergence of the x-ray beam is also a prerequisite when performing grazing incidence XRD. GIXRD is especially beneficial when studying thin films. *In situ* XRD can be used to identify crystalline phases, grain orientation, and grain size of crystalline materials. If the crystallites are randomly orientated in the film, the intensity of the diffraction peaks can be used as a measure of the amount of deposited material. Detailed analysis of the peakwidths in the XRD pattern with the Scherrer equation can yield grain sizes within the deposited film

$$\tau = \frac{K\lambda}{\beta \cos\theta}. \tag{5}$$

Here, τ is the mean size of the ordered crystalline domains, K is a dimensionless shape factor, with a value close to unity depending on the shape of the crystallites, λ is the x-ray wavelength, β is the line broadening at half the maximum intensity in radians, and θ is the Bragg angle.

The use of XRD as an *in situ* technique during ALD allows for a detailed study of, for example, the nucleation of metals, the evolution of grain sizes during growth, the influence of growth conditions on the crystallinity, and the influence of the support (epitaxial growth).

To illustrate the technique, we will again discuss a proof of principle experiment. The *ex situ* XRD patterns for Pt grown on native SiO_2 for 60, 100, and 200 ALD cycles are shown in Fig. 9. The XRD measurements were performed with a Bruker D8 discover system. The Pt has been grown using a thermal ALD process at 150 °C, as described earlier.[47]

The measurements clearly show an increase in intensity of the diffraction peak corresponding with the (111) plane of Pt. A smaller diffraction peak corresponding to the (200) plane is also observed. In the table in Fig. 9, the values for the calculated mean size of the ordered crystalline domains are given for the (111) peak. A clear increase in domain size can be seen. As both the 60 and 100 cycle samples are the exactly same samples studied with GISAXS (as seen in Fig. 7), there is a nice correspondence between both techniques. Both GISAXS and XRD suggest that after 60 ALD cycles, not a lot of platinum is present (low XRD intensity, Yoneda peak at low q_z, corresponding to the critical angle of bare Si) and after 100 ALD cycles the XRD intensity is much larger, indicating platinum has been grown, as is also seen in the shift of the Yoneda peak in the GISAXS pattern to higher q_z values.

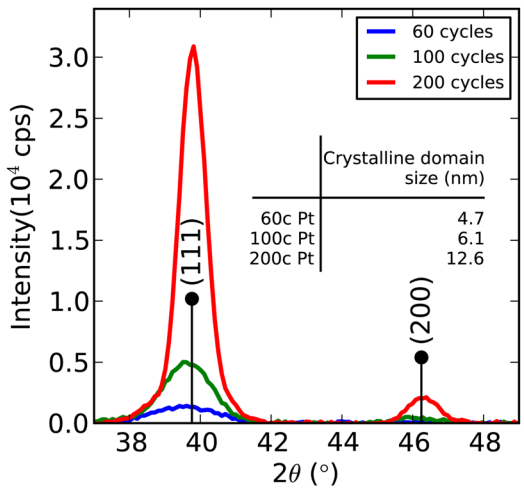

FIG. 9. (Color online) XRD pattern for, respectively, 60, 100, and 200 ALD cycles of Pt growth, showing the (111) and (200) diffraction peak. The inset displays a table of the domain sizes for the (111) peak calculated with the Scherrer equation [Eq. (5)]. A clear increase in domain size can be seen.

V. ELEMENTAL ANALYSIS

A. X-ray fluorescence

X-ray fluorescence (XRF) is a spectroscopy technique that is based on the excitation of core electrons by x-rays. If the energy of the incident photons is larger than the binding energy of a core electron, that electron can be emitted by the atom. This creates a vacancy, which leaves the atom in an excited state. To relax to a more stable state, an electron from an outer shell will be transferred to the vacancy. This will result in the emission of either an x-ray or an Auger electron. The emitted x-ray will have an energy corresponding to the difference in binding energy between the two shells involved. Because every element has a different set of energy levels, each element will have a specific set of fluorescence peaks. These can be used to identify the elements that are being exposed to the x-rays. This in turn allows determination of sample composition.

Because the creation of an Auger electron instead of a fluorescent x-ray is more favorable in lighter elements, the use of XRF is typically limited to elements with an atomic number larger than 11. Moreover, most window materials (Be, kapton) are only sufficiently transparent to x-rays above a certain x-ray energy. This again limits the use of XRF to heavier elements. The efficiency of x-ray absorption is greatly improved when the incident x-ray energy is slightly above the binding energy of the core electrons. The tunability of the x-ray energy at a synchrotron allows tailoring to the specific elements involved in an experiment.

In situ XRF is an interesting tool to study nucleation behavior during ALD and the growth on complex, nonplanar structures.[32,33] The high intensity of the synchrotron beam enables the detection of a very small amount of material. Therefore, *in situ* XRF can be used to study the very first stages of ALD growth, even on planar surfaces. This has been demonstrated for the nucleation of ZnO (Ref. 26) and TiO_2 (Refs. 32 and 33) on Si, and the growth of HfO_2 on Ge and Si.[29] Since XRF directly detects the amount of deposited material, the substrate shape has little to no influence on the measurement. This allows quantification of the amount of deposited material on high aspect ratio surfaces, where other techniques cannot be used to monitor, e.g., film thickness. This was shown for the growth of TiO_2 in porous silica films.[32–34]

The penetration depth of x-rays for energies typically used during XRF is on the order of microns. If the thickness of the studied layers is larger than a few 100 nm, the reabsorption of fluorescent x-rays needs to be taken into account, since this changes the relation between the intensity of the fluorescent x-rays and the amount of material. For the study of planar ALD grown thin films, this is usually not a problem, since the layers are typically much thinner than 100 nm. In the case of complex 3D structures on a support, attention has to be given to this effect, as these structures can have thicknesses of the order of several microns. Special attention also has to be given to the substrate or support itself. If the substrate is excitable by the used x-rays, a lot of fluorescent x-rays will be created related to the substrate, which can saturate the detector. Additionally, some of the x-rays will get scattered on the sample. These elastic (Rayleigh scattering) and inelastic (mostly Compton scattering) scattered x-rays increase the death time of the detector. Both contributions can be minimized by setting the angle between the incident x-rays and the detector to 90°. To optimize the amount of fluorescence reaching the detector, the detector needs to be placed perpendicular to the sample, since the fluorescence will follow Lambert's cosine law. If we take both geometrical conditions into account, a detector position perpendicular to the sample in combination with a small incident angle is to be preferred, ensuring an angle between the incident x-rays and the detector close to 90°. However, a small incident angle creates a large footprint of the x-ray beam on the sample. To limit the loss of signal and unwanted background signals due to illumination of an area larger than the studied sample, the incident angle is usually chosen based on the maximum footprint size in relation to the sample size.

As a first example the nucleation and growth of HfO_2 is monitored for two different starting surfaces. The two studied surfaces are thermally grown SiO_2 and ALD grown Al_2O_3. HfO_2 is grown by thermal ALD at a sample temperature of 250 °C.

A typical XRF spectrum after several cycles of HfO_2 deposition is shown in Fig. 10. This clearly shows that the spectrum consists of lines corresponding to the substrate (Si K_α), the HfO_2 layer (Hf L_α), scattered x-rays (10 keV), and various smaller signals from the sample holder (Co K_α and Fe K_α). The use of synchrotron based x-rays enables the detection of these small quantities of materials.

In Fig. 11, the evolution of the Hf L_α emission line is shown during the first ALD cycles on the SiO_2 surface. By integrating this peak, a measure of the deposited amount of Hf atoms can be obtained. The integrated intensities obtained for both starting surfaces are shown in Fig. 12. On

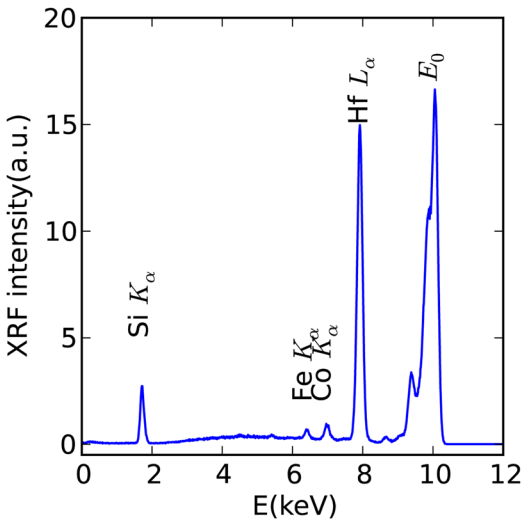

FIG. 10. (Color online) XRF spectrum for 10 ALD cycles of HfO_2 on SiO_2. Lines corresponding to the substrate (Si K_α), the HfO_2 layer (Hf L_α), scattered x-rays (10 keV), and various smaller signals from the sample holder (Co K_α and Fe K_α) can be seen. The use of synchrotron based x-rays enables the detection of these small quantities of materials.

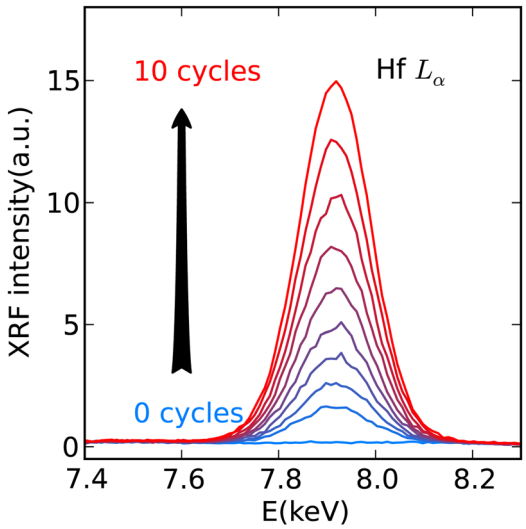

FIG. 11. (Color online) Evolution of the Hf L_α emission line measured during the 10 first ALD cycles of HfO_2 growth on SiO_2.

the ALD grown Al_2O_3 surface, substrate-enhanced growth is observed during the first 10 cycles, likely because the starting surface has a higher density of hydroxyl groups than the growing HfO_2 layer. In contrast, the initial growth on the SiO_2 surface is substrate-inhibited, due to nucleation effects because the starting surface mainly contains oxygen bridges.[1] If we look at the final slope of the growth curves, linear growth is observed, as is expected for ALD. The slope of the growth curve on SiO_2 is almost twice the slope for the growth on Al_2O_3. This means that the GPC is larger on the SiO_2 surface. This can be linked to a higher surface roughness due to the delayed nucleation, which is known to result in rougher films.

Since XRF probes the elemental composition of a material, independent of surface morphology, the technique is ideally suited to study ALD growth on 3D structures. As an example, the thermal growth at 200° of TiO_2 on multiwalled carbon nanotubes (MWCNTs) is shown. In Fig. 13,

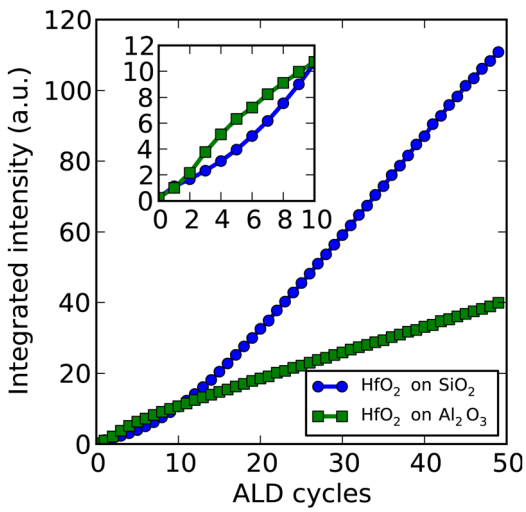

FIG. 12. (Color online) Integrated intensity of the Hf L_α emission line as a function of ALD cycles for the growth of HfO_2 on SiO_2 and Al_2O_3.

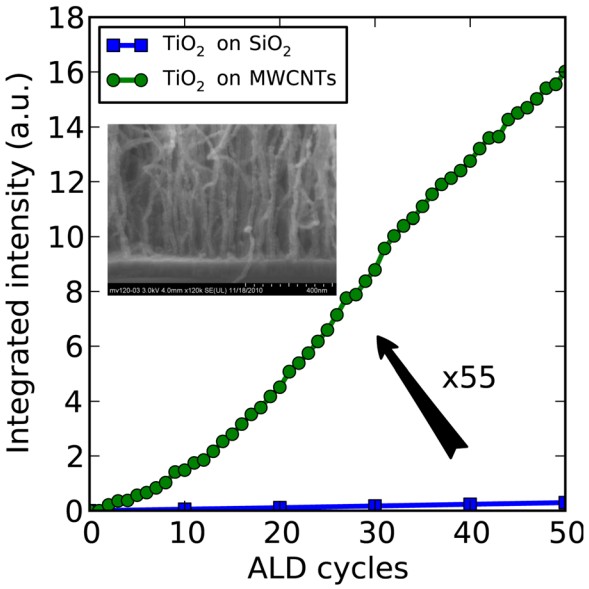

FIG. 13. (Color online) Integrated intensity of the Ti K_α emission line, measured during TiO_2 growth on MWCNTs and a silicon reference. The growth on the MWCNTs has a nucleation period of about 20 ALD cycles. The final slope of the growth curve on the MWCNTs is 55 times larger than the slope of the reference curve, indicating a surface area increase for the MWCNTs as compared to the planar reference. The inset is a SEM picture of the coated MWCNTs, showing a uniform coating on the MWCNTs up to the supporting surface at the bottom.

the integrated intensity of the Ti K_α peak is shown. As a reference, the growth of TiO_2 on native SiO_2 is shown. The data clearly show that a lot more material is deposited on the MWCNTs, compared to a planar reference. This is to be expected, as the surface area of the MWCNTs is several times larger. One can also see that the growth on the MWCNTs has a nucleation period of about 20 ALD cycles. When we now compare the slope for the growth on MWCNTs and the planar reference, the apparent GPC is 55 times larger. The slope can be interpreted as a direct measure for the effective surface area. This allows an estimate of the density of MWCNTS on the sample. The diameter and length of the MWCNTs is known to be 10 nm and 6 μm, respectively. If we assume that the MWCNTs are uniformly coated, a density of 3 10^{10} cm^{-2} is obtained. This is a realistic value suggesting that the MWCNTs are indeed fully coated, as confirmed by cross-sectional SEM.

The use of XRF is not limited to monitoring material that gets added during ALD. It can also be used to analyze etching behavior. Trimethylaluminium (TMA) is known from literature to etch ZnO.[67] We will show this effect with *in situ* XRF measurements. First, a ZnO layer was grown in an anodize alumina substrate. This ensures a larger surface area, resulting in larger signals. In Fig. 14, the evolution of the intensity of the Zn K_α emission line is shown under TMA exposure at 5 10^{-3} mbar. The XRF signal indicates the removal of Zn atoms by TMA.

A final example discusses *in situ* XRF measurements performed during the growth of ZnO in a mesoporous silica film. This is the exact same deposition that was previously discussed in the GISAXS section. The Zn K_α line is

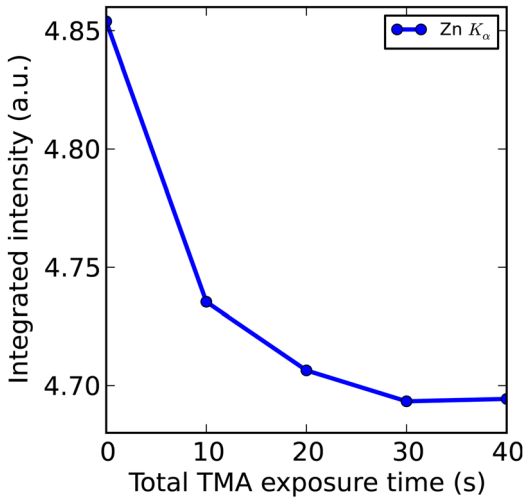

FIG. 14. (Color online) Integrated intensity of the Zn K_α emission line under TMA exposure at 5 10^{-3} mbar, showing the etching behavior of TMA on ZnO.

integrated to monitor the growth in the porous material, as shown in Fig. 15. From the growth curve, it is clear that during the first five cycles a much larger surface is available for ALD growth. During these first ALD cycles, the pores are accessible to the ALD precursors, making the internal surface available for growth. After five ALD cycle the pores are closed to the ALD precursors and growth only continues on top of the porous film, indicated by the lower slope after five ALD cycles.

VI. CHEMICAL ANALYSIS

For completeness, XAS and x-ray photoelectron spectroscopy (XPS) will be briefly introduced. These techniques can provide information about the local chemical state during ALD growth. They have so far not been reported as *in situ* techniques, but are instead used for "*in vacuo*" experiments, where deposition and characterization are performed in separate chambers with vacuum transfer. While the vacuum transfer avoids air exposure, it does impose limitations. The most important being that the transfer of the sample from one chamber to the other obviously takes some time. Since most half reactions during ALD growth generally result in a stable state in UHV, the time in between cycles or half cycles can be increased to allow this transfer. However, certain processes, where the intermediate state after a half reaction is less stable, cannot be studied in this way. An example is the growth of Pt with a N_2 or NH_3 plasma. In this case, the active species on the surface are removed over time.[68] This only allows for a small time window in between (half-) cycles to perform *in vacuo* measurements. A second consideration has to be made with regard to sample temperature during transfer and analysis. The amount of surface groups is known to depend on the sample temperature. Most ALD processes are dependent on the interaction with these groups. This implies that changes in sample temperature during transfer and analysis can have a significant influence on the ALD process. By addressing these issues, an *in vacuo* experiment may provide useful insights, not accessible with true *in situ* techniques. The discussion of XAS and XPS will be limited to a general introduction and a brief prospect of the *in situ* use of these techniques.

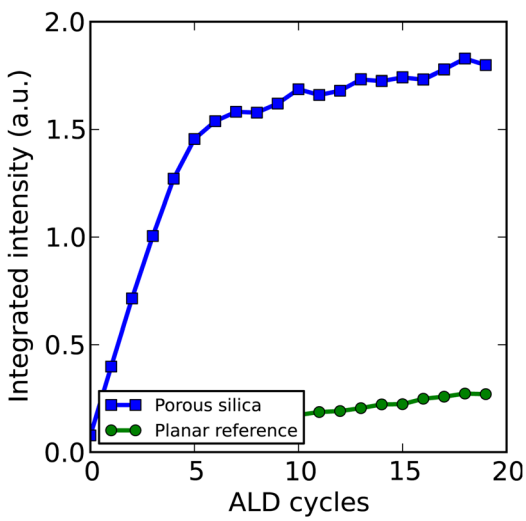

FIG. 15. (Color online) Integrated intensity of the Zn K_α emission line during growth of ZnO in a porous silica film. During the first five cycles growth is occurring on the internal surface, indicated by the larger slope. After five cycles, ZnO is grown on top of the film. The growth on a planar Si surface is shown as a reference.

A. X-ray absorption spectroscopy

In x-ray absorption spectroscopy (XAS) one measures the absorption of x-rays by a material as a function of energy to obtain detailed structural and electronic information through extended x-ray absorption fine structure (EXAFS) and x-ray absorption near edge structure, respectively.[69] Classically, XAS is performed by looking at the transmitted x-ray intensity through a material. The transmission is then given by the Beer-Lambert law

$$I_t = I_0 e^{-\mu(E)t} \tag{6}$$

with the absorption coefficient $\mu(E)$ as function of the energy and the thickness of the material t. Generally x-ray absorption decreases smoothly for increasing energy. But if the energy of the x-rays becomes large enough, an electron from an inner shell of the material can be excited, as already explained for XRF. This will give rise to a sharp increase in absorption at the specific binding energy of the core electron. This increase is denoted as the absorption edge or threshold energy. The emitted electron will have a kinetic energy ($E_{kinetic}$) corresponding to the photoelectric effect

$$E_{\text{kinetic}} = h\nu - E_{\text{binding}}. \tag{7}$$

Quantum mechanically the outgoing photoelectron can be represented as a spherical wave. This wave will scatter on the surrounding atoms (specifically the electron densities), producing a backscattered wave. These outgoing and backscattered waves interfere, causing an interference pattern. The distance to the neighboring atoms determines the

interference pattern. As a result, the absorption coefficient above the absorption edge is defined as

$$\mu = \mu_0 + \chi_{(EX)} \tag{8}$$

with μ_0 representing the atomic background. $\chi_{(EX)}$ describes the scattering of the outgoing electron against the neighboring atoms. It is called the EXAFS function. This oscillatory part of the absorption coefficient contains information about the local structure around the absorber atom. Since the electrons only get excited around a specific energy, XAS is element specific.

As an alternative to measuring the x-ray transmission, the fluorescence can be studied. Since the fluorescence intensity is closely related to the absorption coefficient, the same information can be obtained. This is important when we want to apply XAS as an *in situ* technique during ALD. When studying thin films, an absorption measurement will only see a very small change in transmission, due to the limited amount of absorbing material in the film. This will result in a low signal to noise ratio. The fluorescent signal on the other hand will even be available when only little material is present.

The use of XAS has been reported as an *ex situ* technique.[70–72] There are also reports of XAS as an *in vacuo* technique, where the sample can be transferred from the ALD chamber to an UHV system to allow for XAS.[36–39] To the best of our knowledge, the use of XAS as an *in situ* technique has been performed once on powderous supports in absorption mode[40] and once studying ALD growth on a planar support in fluorescence mode.[41]

B. X-ray photoelectron spectroscopy

XPS is a technique that allows the study of composition and chemical state of the elements in a material. XPS is based on the photoelectric effect [Eq. (7)]. The material gets illuminated with x-rays at a fixed energy (E_{photon}). These x-rays will interact with the electrons in the shells of the illuminated atoms. These electrons can get emitted if E_{photon} is larger than the electron binding energy ($E_{binding}$). The surplus in energy will be converted into kinetic energy ($E_{kinetic}$) of the photo electron. These electrons can then be collected and analyzed. This leads to the following equation used for XPS analysis:

$$E_{\text{binding}} = E_{\text{photon}} - (E_{\text{kinetic}} - \Phi). \tag{9}$$

Here, Φ is the work function of the spectrometer. Every element has a characteristic set of peaks at specific $E_{binding}$. This allows for an elemental analysis of a sample. As $E_{binding}$ also depends on the chemical state of the involved atoms, XPS can be used to determine the local bonding of atoms.

Since only electrons created at the surface exit the material unaltered, the information depth of XPS is limited to a few nanometers. From an ALD point of view, this can be considered an advantage for *in situ* analysis, since we are only interested in the very top surface. Because XPS is based on the collection of electrons, UHV is needed. This is a very important hurdle when it comes to implementing XPS as an *in situ* technique. Moreover, fragile detection electronics are in direct contact with the vacuum of the analysis chamber. If we would implement ALD inside an XPS chamber, the UHV conditions would be very hard to achieve and special care would have to be made to protect the detector from the ALD process. This directly explains why no use of XPS as *in situ* technique has been reported in literature. There are however several examples of the use of XPS as *in vacuo* technique, meaning that the sample gets transferred from an ALD chamber to an XPS analysis chamber under UHV conditions.[37,38,42–45] However, the development of high pressure XPS and ambient pressure XPS systems, as are currently pioneered for *in situ* studies during catalysis, could make *in situ* XPS possible under ALD conditions.[73]

VII. PRACTICAL CONSIDERATIONS OF SYNCHROTRON USE

The use of synchrotron radiation obviously also comes with a few disadvantages. If the flux on the sample is too high and the sample is sensitive to x-rays, the surface might get altered, changing the ALD process that is being monitored. Limiting the flux to the sample, increasing the footprint of the x-ray beam, and blocking the sample from x-rays when no measurements are being performed reduce the x-ray effects. Possible decomposition of the gas molecules by x-rays can be avoided by only allowing illumination when the reactor has been purged/pumped.

Second, at least two x-ray transparent windows need to be incorporated into the reactor design. Because of the conformal nature of ALD, these windows either need to be protected by valves during gas exposures or need to be considered as consumables. Since in most cases the temperature of the windows will be limited, either by heating efficiency and/or the practical upper limit to the allowed temperature of the window, in practice, most ALD processes will deposit very little material on the windows.

Third, since synchrotron facilities only have a limited amount of available time compared to the demand from various scientific areas, a request has to be made for experimental time. Due to selection procedures and scheduling, in most cases, a few months up to more than half a year can pass between application for experimental time and the actual experiment. Additionally, as a multiuser facility, safety is a key issue at a synchrotron facility, both concerning the involved chemicals and the interface between the beamline equipment and the *in situ* ALD reactor. Communication with beamline staff can be of great help to make an estimate of the feasibility of your experiment at a specific facility.

VIII. REACTOR DESIGN

Design of an ALD reactor that allows for *in situ* synchrotron studies asks for some specific adaptations and changes to a standard ALD reactor. A lot of experience exists within the field of catalysis, where a multitude of operando reaction cells have been designed over the last decades for operando EXAFS or XRD during catalytic reactions. These reaction

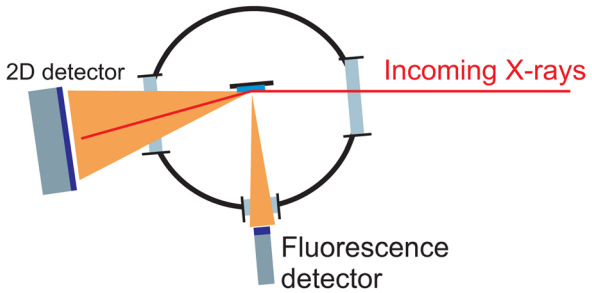

FIG. 16. (Color online) Schematic view of an ALD chamber for *in situ* x-ray experiments.

cells typically use a heating stage to heat the catalyst up to 500 °C and work under a wide range of gas ambients.[74–76] This can be translated to an ALD design, where typically similar requirements need to be met. In Fig. 16, a schematic representation of an ALD chamber, adapted for various *in situ* synchrotron based techniques is shown.

Currently, several chambers have already been used to perform x-ray studies during ALD, both flow type reactors,[24,26] and pump type reactors.[29,32–34] A few issues that need to be addressed when adapting or designing these chambers will be briefly discussed.

As the x-ray source in the case of synchrotron experiments is fixed, changing the incident angle needs to be achieved by either mounting the full ALD chamber on a movable stage and/or incorporating a movable sample stage into the design. Even if only measurements at a fixed position will be performed, still some rotational and/or translational freedom is required, in order to align the x-ray beam with the chamber.

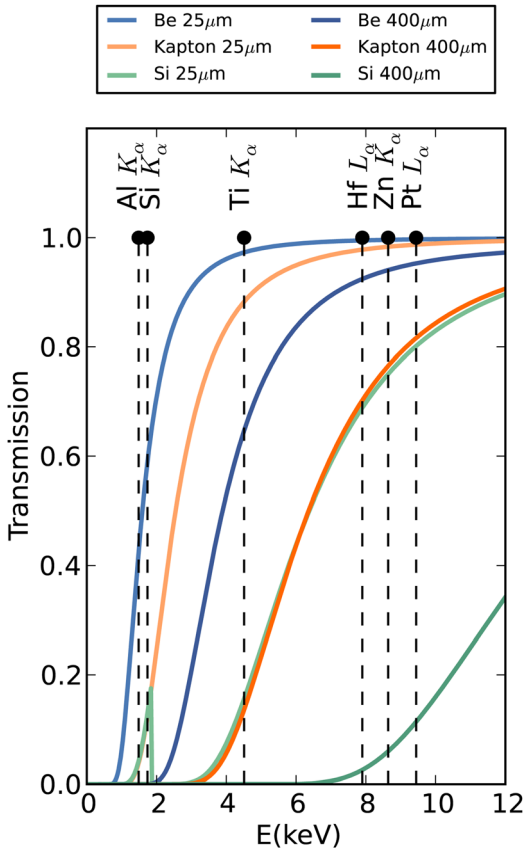

FIG. 17. (Color online) Transmission for Be, Kapton and Silicon of a thickness of 25 μm and 400 μm. Some fluorescent lines are added for materials that are frequently grown by ALD.

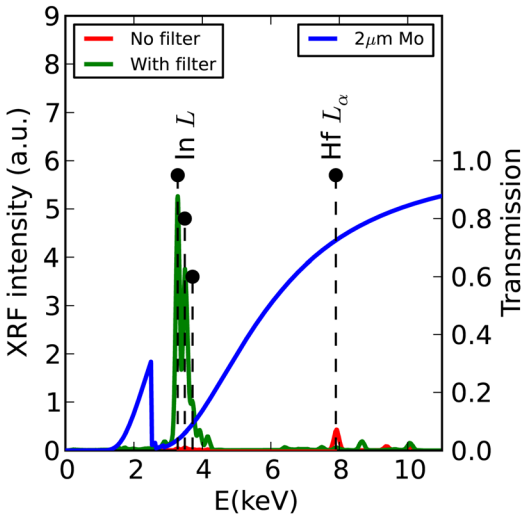

FIG. 18. (Color online) XRF spectrum for a HfO_2 layer on InP, with and without molybdenum filter. The theoretical transmission of the Mo filter is overlayed. Without filter, only indium and no hafnium can be detected. With filter, the Hf L_α line is clearly visible and the In L lines are greatly reduced.

Windows need to be incorporated into the chamber design to allow x-rays to pass from the source to the sample and back to a detector. In most cases, either beryllium or kapton windows are used as these materials are sufficiently transparent in the keV energy range. The transmission of both materials is shown in Fig. 17 for typical window thicknesses. The transmission of silicon is added for comparison. In general, thinner windows are preferred, because they allow for the highest transmission. However, depending on the size of the needed window, the strength of the window needs to be taken into account, as in most cases, the window needs to withstand around one atmosphere in pressure difference. This directly results in a minimal window thickness for a given diameter.

Clever use of the x-ray transmission properties of various materials is not limited to the selection of window materials. If unwanted x-rays at a specific energy are preventing accurate *in situ* measurements, a filter material can be placed either directly in front of the entrance window or in front of the detector. As an example, the effect of a molybdenum filter on the fluorescent spectrum of an ALD grown HfO_2 layer on InP is shown in Fig. 18. Without the filter, the fluorescence from the indium saturates the detector, resulting in a spectrum where only indium can be detected. If a 2 μm thick Mo filter is positioned in front of the fluorescence detector, most of the x-rays at energies below 5 keV are blocked, reducing the amount of fluorescence from the In substrate reaching the detector. On the other hand, the fluorescence coming from the Hf atoms in the HfO_2 layer are only partially absorbed. This results in a detectable Hf L_α line,

without saturating the detector, allowing the study of HfO_2 growth on InP with *in situ* XRF.

IX. CONCLUSIONS

Extending the wavelength range of optical *in situ* techniques to x-rays enables the use of XRR, XRF, and XPS during ALD. This expands the information available in the study of layer growth during ALD, both on planar and on complex structures. The use of synchrotron based x-rays is beneficial to *in situ* studies, because of the high photon flux and the energy tunability, enabling GISAXS and XAS.

All these techniques are especially sensitive to changes on the (sub-) nanometer scale. As the changes during growth are typically of this order, they are ideally suited for *in situ* studies of ALD. The range of x-ray techniques available allows the study of specific facets of the processes involved in ALD. These techniques can complement well established techniques in determining, e.g., thicknesses, densities, and crystallinity and/or provide *in situ* information, unavailable to other techniques, e.g., morphology.

In short, *in situ* synchrotron based x-ray techniques form a new set of valuable tools in monitoring atomic layer deposition.

ACKNOWLEDGMENTS

The research leading to these results has received funding from the European Research Council under the European Union's Seventh Framework Programme (FP7/2007–2013)/ERC grant agreement no. 239865. Christophe Detavernier and Jolien Dendooven also acknowledge funding by FWO-Vlaanderen, BOF-UGent and GOA no. 01G01513. Karl Ludwig acknowledges funding by the U.S. Department of Energy, under Contract no. DE-FG02-03ER46037. Use of the National Synchrotron Light Source, Brookhaven National Laboratory, was supported by the U.S. Department of Energy, Office of Science, Office of Basic Energy Sciences, under Contract no. DE-AC02-98CH10886.

[1]R. L. Puurunen, J. Appl. Phys. **97**, 121301 (2005).
[2]S. M. George, Chem. Rev. **110**, 111 (2010).
[3]C. Detavernier, J. Dendooven, S. P. Sree, K. F. Ludwig, and J. A. Martens, Chem. Soc. Rev. **40**, 5242 (2011).
[4]V. Miikkulainen, M. Leskela, M. Ritala, and R. L. Puurunen, J. Appl. Phys. **113**, 021301 (2013).
[5]J. W. Elam, M. D. Groner, and S. M. George, Rev. Sci. Instrum. **73**, 2981 (2002).
[6]M. N. Rocklein and S. M. George, Anal. Chem. **75**, 4975 (2003).
[7]A. Rahtu and M. Ritala, Chem. Vapor Depos. **8**, 21 (2002).
[8]R. Matero, A. Rahtu, and M. Ritala, Chem. Mater. **13**, 4506 (2001).
[9]M. Schuisky, J. W. Elam, and S. M. George, Appl. Phys. Lett. **81**, 180 (2002).
[10]O. Nilsen and H. Fjellvåg, J. Therm. Anal. Calorim. **105**, 33 (2011).
[11]M. Juppo, A. Rahtu, M. Ritala, and M. Leskelä, Langmuir **16**, 4034 (2000).
[12]H. Kim, A. J. Kellock, and S. M. Rossnagel, J. Appl. Phys. **92**, 7080 (2002).
[13]A. J. M. Mackus, S. B. S. Heil, E. Langereis, H. C. M. Knoops, M. C. M. van de Sanden, and W. M. M. Kessels, J. Vac. Sci. Technol. A **28**, 77 (2010).
[14]R. K. Grubbs, N. J. Steinmetz, and S. M. George, J. Vac. Sci. Technol. B **22**, 1811 (2004).
[15]N. Kobayashi and Y. Kobayashi, Thin Solid Films **225**, 32 (1993).
[16]K. Nishi, A. Usui, and H. Sakaki, Appl. Phys. Lett. **61**, 31 (1992).
[17]J. W. Klaus, S. J. Ferro, and S. M. George, J. Electrochem. Soc. **147**, 1175 (2000).
[18]S. Yokoyama, H. Goto, T. Miyamoto, N. Ikeda, and K. Shibahara, Appl. Surf. Sci. **112**, 75 (1997).
[19]A. C. Dillon, A. Ott, J. Way, and S. M. George, Surf. Sci. **322**, 230 (1995).
[20]E. Langereis, S. B. S. Heil, M. C. M. van de Sanden, and W. M. M. Kessels, J. Appl. Phys. **100**, 023534 (2006).
[21]J. Dendooven, K. Devloo-Casier, E. Levrau, R. Van Hove, S. P. Sree, M. R. Baklanov, J. A. Martens, and C. Detavernier, Langmuir **28**, 3852 (2012).
[22]Y. Hwang, K. Heo, C. H. Chang, M. K. Joo, and M. Ree, Thin Solid Films **510**, 159 (2006).
[23]J. P. Yong, R. L. Dong, and B. Sunggi, J. Korean Phys. Soc. **59**, 458 (2011).
[24]Y. J. Park, D. R. Lee, H. H. Lee, H.-B.-R. Lee, H. Kim, G.-C. Park, S.-W. Rhee, and S. Baik, J. Nanosci. Nanotechnol. **11**, 1577 (2011).
[25]T.-B. Hur, Y.-H. Hwang, H.-K. Kim, and H.-L. Park, J. Appl. Phys. **96**, 1740 (2004).
[26]D. D. Fong, J. a. Eastman, S. K. Kim, T. T. Fister, M. J. Highland, P. M. Baldo, and P. H. Fuoss, Appl. Phys. Lett. **97**, 191904 (2010).
[27]H.-B.-R. Lee, Y. J. Park, S. Baik, and H. Kim, Chem. Vap. Depos. **18**, 41 (2012).
[28]J. Dendooven, K. Devloo-Casier, M. Ide, K. Grandfield, K. F. Ludwig, S. Bals, P. Van Der Voort, and C. Detavernier, ECS Trans. **50**, 35 (2013).
[29]K. Devloo-Casier, J. Dendooven, K. F. Ludwig, G. Lekens, J. Dhaen, and C. Detavernier, Appl. Phys. Lett. **98**, 231905 (2011).
[30]S.-J. Park, W.-H. Kim, W. Maeng, Y. Yang, C. Park, H. Kim, K.-N. Lee, S.-W. Jung, and W. Seong, Thin Solid Films **516**, 7345 (2008).
[31]R. Methaapanon, S. M. Geyer, S. Brennan, and S. F. Bent, Chem. Mater. **25**, 3458 (2013).
[32]J. Dendooven, D. Deduytsche, S. Pulinthanathu Sree, T. Korànyi, G. Vanbutsele, J. A. Martens, K. F. Ludwig, and C. Detavernier, *AVS Topical Conference on ALD*, Seoul, South Korea (2010).
[33]J. Dendooven, S. Pulinthanathu Sree, K. De Keyser, D. Deduytsche, J. A. Martens, K. F. Ludwig, and C. Detavernier, J. Phys. Chem. C **115**, 6605 (2011).
[34]J. Dendooven *et al.*, Chem. Mater. **24**, 1992 (2012).
[35]E. Levrau, K. Devloo-Casier, J. Dendooven, K. F. Ludwig, P. Verdonck, J. Meersschaut, M. R. Baklanov, and C. Detavernier, Langmuir **29**, 12284 (2013).
[36]M. Tallarida, K. Karavaev, and D. Schmeisser, J. Appl. Phys. **104**, 064116 (2008).
[37]M. Tallarida and D. Schmeisser, Semicond. Sci. Technol. **27**, 074010 (2012).
[38]R. Methaapanon, S. M. Geyer, C. Hagglund, P. a. Pianetta, and S. F. Bent, Rev. Sci. Instrum. **84**, 015104 (2013).
[39]M. Tallarida, K. Karavaev, and D. Schmeisser, J. Vac. Sci. Technol. B **27**, 300 (2009).
[40]W. Setthapun *et al.*, J. Phys. Chem. C **114**, 9758 (2010).
[41]M. Filez, H. Poelman, R. K. Ramachandran, J. Dendooven, K. Devloo-Casier, E. Fonda, C. Detavernier, and G. B. Marin, *European Materials Research Society (E-MRS) Spring Meeting 2013* (2013).
[42]S. M. Geyer, R. Methaapanon, B. Shong, P. a. Pianetta, S. F. Bent, and A. Piero, J. Phys. Chem. Lett. **4**, 176 (2013).
[43]M. Kobayashi, P. T. Chen, Y. Sun, N. Goel, P. Majhi, M. Garner, W. Tsai, P. Pianetta, and Y. Nishi, Appl. Phys. Lett. **93**, 182103 (2008).
[44]K. Kolanek, M. Tallarida, M. Michling, and D. Schmeisser, J. Vac. Sci. Technol. A **30**, 01A143 (2012).
[45]M. Tallarida, C. Adelmann, A. Delabie, S. V. Elshocht, M. Caymax, and D. Schmeisser, IOP Conf. Ser.: Mater. Eng. **41**, 012003 (2012).
[46]G. Ozaydin, A. S. Ozcan, Y. Wang, K. F. Ludwig, H. Zhou, R. L. Headrick, and D. P. Siddons, Appl. Phys. Lett. **87**, 163104 (2005).
[47]J. Dendooven, R. K. Ramachandran, K. Devloo-Casier, G. Rampelberg, M. Filez, H. Poelman, G. B. Marin, E. Fonda, and C. Detavernier, J. Phys. Chem. C **117**, 20557 (2013).
[48]P. Croce, G. Devant, M. Sere, and M. Verhaeghe, Surf. Sci. **22**, 173 (1970).
[49]E. Chason and T. M. Mayer, Crit. Rev. Solid State Mater. Sci. **22**, 1 (1997).
[50]L. Parratt, Phys. Rev. **95**, 359 (1954).
[51]J. R. Levine, J. B. Cohen, Y. W. Chung, and P. Georgopoulos, J. Appl Crystallogr. **22**, 528 (1989).

[52]G. Renaud, R. Lazzari, and F. Leroy, Surf. Sci. Rep. **64**, 255 (2009).
[53]D. Heggie and R. Mathieu, *Lecture Notes in Physics*, edited by J. Daillant and A. Gibaud, Lecture Notes in Physics, Vol. 770 (Springer, Berlin, 2009).
[54]Y. Yoneda, Phys. Rev. **131**, 2010 (1963).
[55]S. Dourdain, J.-F. Bardeau, M. Colas, B. Smarsly, A. Mehdi, B. M. Ocko, and A. Gibaud, Appl. Phys. Lett. **86**, 113108 (2005).
[56]G. Renaud *et al*., Science **300**, 1416 (2003).
[57]G. Ozaydin, K. F. Ludwig, H. Zhou, L. Zhou, and R. L. Headrick, J. Appl. Phys. **103**, 033512 (2008).
[58]S. T. Christensen, J. W. Elam, B. Lee, Z. Feng, M. J. Bedzyk, and M. C. Hersam, Chem. Mater. **21**, 516 (2009).
[59]R. Lazzari, J. Appl. Crystallogr. **35**, 406 (2002).
[60]J. Dendooven, *Modeling and In Situ Characterization of the Conformality of Atomic Layer Deposition in High Aspect Ratio Structures and Nanoporous Materials* (Ghent University, Faculty of Sciences, 2012).
[61]V. Lujala, J. Skarp, M. Tammenmaa, and T. Suntola, Appl. Surf. Sci. **82–83**, 34 (1994).
[62]N. Terasawa *et al*., Appl. Surf. Sci. **244**, 16 (2005).
[63]H.-B.-R. Lee and H. Kim, Electrochem. Solid State **9**, G323 (2006).
[64]W.-H. Kim, H.-B.-R. Lee, K. Heo, Y. K. Lee, T.-M. Chung, C. G. Kim, S. Hong, J. Heo, and H. Kim, J. Electrochem. Soc. **158**, D1 (2011).
[65]P. Alén, "Atomic layer deposition of TaN, NbN, and MoN films for Cu metallizations," Academic Dissertation (University of Helsinki, 2005).
[66]L. Borgese, M. Gelfi, E. Bontempi, P. Goudeau, G. Geandier, D. Thiaudière, and L. Depero, Surf. Coat. Technol. **206**, 2459 (2012).
[67]J. W. Elam and S. M. George, Chem. Mater. **15**, 1020 (2003).
[68]D. Longrie, K. Devloo-Casier, D. Deduytsche, S. Van den Berghe, K. Driesen, and C. Detavernier, ECS J. Solid State Sci. Technol. **1**, Q123 (2012).
[69]D. Koningsberger and B. Mojet, Top. Catal. **10**, 143 (2000).
[70]M. Han, Y. Luo, J. Moryl, R. Osgood, and J. Chen, Surf. Sci. **415**, 251 (1998).
[71]S. T. Christensen, H. Feng, J. L. Libera, N. Guo, J. T. Miller, P. C. Stair, and J. W. Elam, Nano Lett. **10**, 3047 (2010).
[72]S. T. Christensen *et al*., Small **5**, 750 (2009).
[73]D. Teschner, A. Pestryakov, E. Kleimenov, M. Havecker, H. Bluhm, H. Sauer, A. Knopgericke, and R. Schlogl, J. Catal. **230**, 186 (2005).
[74]T. Shido and R. Prins, Curr. Opin. Solid State Mater. Sci. **3**, 330 (1998).
[75]X. Wang, J. a. Rodriguez, J. C. Hanson, M. Pérez, and J. Evans, J. Chem. Phys. **123**, 221101 (2005).
[76]G. Sankar and J. M. Thomas, Top. Catal. **8**, 1 (1999).